nature astronomy

Article

https://doi.org/10.1038/s41550-024-02319-3

Heterogeneous outgassing regions identified on active centaur 29P/Schwassmann–Wachmann 1

Received: 1 March 2024

Accepted: 13 June 2024

Published online: 08 July 2024

Check for updates

Sara Faggi[1,2] ✉, Geronimo L. Villanueva[1], Adam McKay[3], Olga Harrington Pinto[4,5], Michael S. P. Kelley[6], Dominique Bockelée-Morvan[7], Maria Womack[5,8], Charles A. Schambeau[5], Lori Feaga[6], Michael A. DiSanti[1], James M. Bauer[6], Nicolas Biver[7], Kacper Wierzchos[9] & Yanga R. Fernandez[5]

Centaurs are transitional objects between primitive trans-Neptunian objects and Jupiter-family comets. Their compositions and activities provide fundamental clues regarding the processes affecting the evolution of and interplay between these small bodies. Here we report observations of centaur 29P/Schwassmann–Wachmann 1 (29P) with the James Webb Space Telescope (JWST). We identified localized jets with heterogeneous compositions driving the outgassing activity. We employed the NIRSpec mapping spectrometer to study the fluorescence emissions of CO and obtain a definitive detection of CO_2 for this target. The exquisite sensitivity of the instrument also enabled carbon and oxygen isotopic signatures to be probed. Molecular maps reveal complex outgassing distributions, such as jets and anisotropic morphology, which indicate that 29P's nucleus is dominated by active regions with heterogeneous compositions. These distributions could reflect that it has a bilobate structure with compositionally distinct components or that strong differential erosion takes place on the nucleus. As there are no missions currently planning to visit a centaur, these observations demonstrate JWST's unique capabilities in characterizing these objects.

Centaurs are a transitional class of small bodies with orbits between Jupiter and Neptune and relatively short dynamical lifetimes of about 1–10 Myr. Dynamical models show that centaurs are former trans-Neptunian objects (TNOs). Most originated from the dynamically hot (or scattered) population of TNOs[1–7], with smaller contributions from other populations[8–15]. They consequently evolved to have Neptune-encountering orbits that scattered them inwards into the region of giant planets, where gravitational interactions either ejected them back into the TNO scattering population or transferred them into the population of Jupiter-family comets (JFCs), whose aphelia are near Jupiter's orbit[2,6–8,16].

Although TNOs are generally considered to be inactive bodies and are thought to be made of primordial ices that reflect the composition of the protoplanetary disk regions where they formed[17–21], JFCs have been substantially thermally processed due to the numerous close encounters with the Sun. These encounters periodically

[1]NASA Goddard Space Flight Center, Greenbelt, MD, USA. [2]American University, Washington, DC, USA. [3]Appalachian State University, Boone, NC, USA. [4]Auburn University, Auburn, AL, USA. [5]University of Central Florida, Orlando, FL, USA. [6]University of Maryland, College Park, MD, USA. [7]LESIA, Observatoire de Paris, Université PSL, Sorbonne Université, Université Paris Cité, CNRS, Meudon, France. [8]National Science Foundation, Alexandria, VA, USA. [9]University of Arizona, Tucson, AZ, USA. ✉e-mail: sara.faggi@nasa.gov

expose their ices to high temperatures. The composition of JFCs is then a combination of their natal conditions in their birthplace, the unique outgassing evolutionary history experienced during their transitional phase as centaurs and their current periodic activity[19,22,23]. Being the intermediate stage in the orbital evolution from TNOs to JFCs, the nuclear ices of most centaurs have not yet suffered the frequent, strong and repeated thermal processing that is experienced by JFCs, although it has been shown that a few centaurs might have endured short-term JFC orbits with solar heating and processing and then moved out into the centaur gateway region again[24]. An important example is 39P/Oterma, a centaur whose orbit was temporarily inside Jupiter's and shows a distinct chemical composition compared to the centaur 29P/Schwassmann–Wachmann 1 (29P), possibly due to the different level of thermal processing[25]. Investigations of the composition of centaurs is, therefore, of key importance for revealing the drivers of activity in icy bodies at large heliocentric distances, for understanding how their nuclear ices get shaped and for connecting the compositional diversity of the TNO population (heritage) to the observed properties (evolutionary) of periodic comets (for example, strong depletion in volatile species such as CO, relative to long-period comets (LPCs)).

The morphology of cometary comae has been investigated for decades through imaging at optical wavelengths, by employing narrow-band filters[26–28] and lately also with integral field unit (IFU) techniques[29]. In the optical, only a small number of radical species is detectable (fragments of parent molecules, primarily those released from the sublimation of nuclear ices), yet despite this, such imaging provides important information about the nucleus properties (for example, rotation). However, data about radical species cannot deliver a comprehensive picture of the nucleus composition. Investigations of the morphology of dust comae and the spatial distribution of the gas species have been performed at longer wavelengths[30–35] (for example, millimetre or submillimetre), but the mapped information is limited in spatial resolution. Direct investigations on how ices are stored in the nuclei of comets and centaurs can be performed only by space missions (for example, Deep Impact, EPOXI and Rosetta) that can resolve the nucleus and map its surface and volatiles[36–40], even if these investigations can be performed only for a limited number of objects. As no missions are currently planning to visit a centaur, indirect investigations of their activity through remote sensing, which targets the spatial distributions of the sublimating nuclear volatile ices released from the coma (parent molecules), are the only way to access these objects and infer the heterogeneity of their nuclei. Unfortunately, very little is known about the dominant mechanisms driving the outgassing activity of centaurs. With perihelion distances greater than 4 au, water sublimation can probably be excluded as the main driver (as it occurs only to trace degrees outside 2–3 au), leading to two proposed theories supported by modelling efforts: (1) activity driven by hypervolatile species, such as CO or CO_2, which are stored as pockets of nuclear ices underneath the surface and undergo sublimation once exposed and (2) activity driven by pockets of amorphous water ice that undergo the crystalline state transition, releasing CO or CO_2 previously incorporated in the ice in gaseous form[41–46].

The three most abundant parent molecules in comets (H_2O, CO and CO_2) have strong fluorescence bands in the infrared that are inaccessible to ground-based observatories due to the lack of atmospheric transparency, which restricts sensitive searches for these species in faint objects. In addition, spectroscopic observations of centaurs, such as 29P (refs. 34,35,47,48), 2060 Chiron (refs. 49–51) and 174P/Echeclus (ref. 52), are particularly challenging due to the typically large heliocentric and geocentric distances, which dilutes the fluxes greatly. Ultimately, this requires unprecedented sensitivities, such as those provided by a cryogenic space observatory like the James Webb Space Telescope (JWST). The JWST advanced infrared instrumentation uniquely favours the study of these objects by providing orders of magnitude improvements in sensitivity and spatial resolution compared to what is possible with other observatories. Moreover, JWST is the only extant platform capable of distinguishing between CO and CO_2 fluorescence emissions at infrared wavelengths. On 20 February 2023 UT, we observed centaur 29P with JWST as part of the cycle 1 programme 2416 (ref. 53). We used the PRISM IFU of the near-infrared spectrograph (NIRSpec)[54,55]. This instrument delivered a data cube across a uniform spaxel (spatial pixel) size of 0.1″ × 0.1″ across a 3″ × 3″ field of view (FoV) ('Observations and data reduction' in Methods). The JWST/NIRSpec observations covered the 0.6 to 5.3 μm wavelength region at a resolving power of ~100, which allowed us to probe the fluorescence emission bands of H_2O at 2.7 μm, CO_2 at 4.3 μm and CO at 4.7 μm and several isotopologues of these species (for example, $^{13}CO_2$, ^{13}CO, $C^{17}O$ and $C^{18}O$).

Figure 1 presents flux-calibrated spectra for the integrated signal across a 0.9″-length-box aperture (Fig. 1a). Molecular emissions in the 4–5 μm region of several isotopologues of CO_2 and CO (Fig. 1a,b,f) were identified. Beyond these strong molecular emission features, the 29P spectrum also displays organic molecular emissions at 3.3 μm and strong surface ice absorption features, including a notable 3 μm absorption (without the Fresnel peak at 3.1 μm) and other absorptions at shorter wavelengths. Neither CO_2 or CO ice was clearly identified, nor were water gas emission features detected. As such, these are not discussed further in this paper. Further details of the surface composition, analysis of the dust continuum fluxes and the organic molecular inventory of 29P as measured with JWST will be presented in subsequent investigations.

Heterogeneous outgassing of CO and CO_2

To quantify the spatial distributions of CO and CO_2 outgassing, we analysed a selected portion of the full spectrum covering the 4–5 μm wavelength region (Fig. 1b), and we performed spaxel-by-spaxel retrievals using the Planetary Spectrum Generator (PSG)[56,57]. PSG includes advanced excitation models for these species and incorporates photodissociation decay, while adopting an optically thick treatment for the non-local-thermodynamic-equilibrium fluorescence models. The latter was essential for obtaining reliable estimates of the number of molecules encompassed by each spaxel FoV (Fig. 1c–e). Regarding the excitation state, we derived a rotational temperature of (4.5 ± 1) K from the shape of the CO and CO_2 emission bands presented in Fig. 1b, which is consistent with previous measurements[34,35,47,48]. This temperature refers to the molecular rotational-vibrational excitation temperature, which is close to the ambient kinetic temperature of CO, as measured by radio observations[35], and of CO_2 gases. The CO and CO_2 maps of column density were extracted from a 21 × 21 spaxel box (2.1″ × 2.1″) using a region of ±10 spaxels along the north–south and east–west directions and centred on the brightest photometric spaxels where 29P's nucleus is located. This region is shown in the light blue box in Fig. 1a. For each spaxel retrieval, the rotational temperature was kept fixed at 4.5 K, a second-order polynomial function was applied to fit the continuum between 4 and 5 μm and the isotopic abundances were set to telluric values[58,59]: $CO_2/^{13}CO_2 = 89$, $CO/^{13}CO = 89$, $CO/C^{17}O = 2{,}682$ and $CO/C^{18}O = 500$. This allowed us to achieve non-resonant multi-band and multi-isotope self-consistent fluorescence radiative-transfer modelling of the coma. We also explored possible deviations from telluric isotopic ratios ('Observations and data reduction' in Methods).

The retrieved molecular gas density maps show that highly collimated jets are being emitted from 29P (Fig. 2). To compensate for expansion dilution, the retrieved column density maps (m^{-2}) were divided by $1/\rho$ (m^{-1}), where ρ is the sky-plane projected distance form the nucleus in metres, thus highlighting the asymmetric nature of the coma outflow. This technique is commonly used in comet image enhancement[26,60]. The retrieved column densities (m^{-2}) are also presented in 'KAMJO details' in Methods. There is a jet of CO outflowing towards the north, whereas CO_2 shows instead a very different outgassing morphology, as it has two jets flowing in opposite directions, north and south. Outside these lateral jets, we also observed a constant $1/\rho$

https://doi.org/10.1038/s41550-024-02319-3

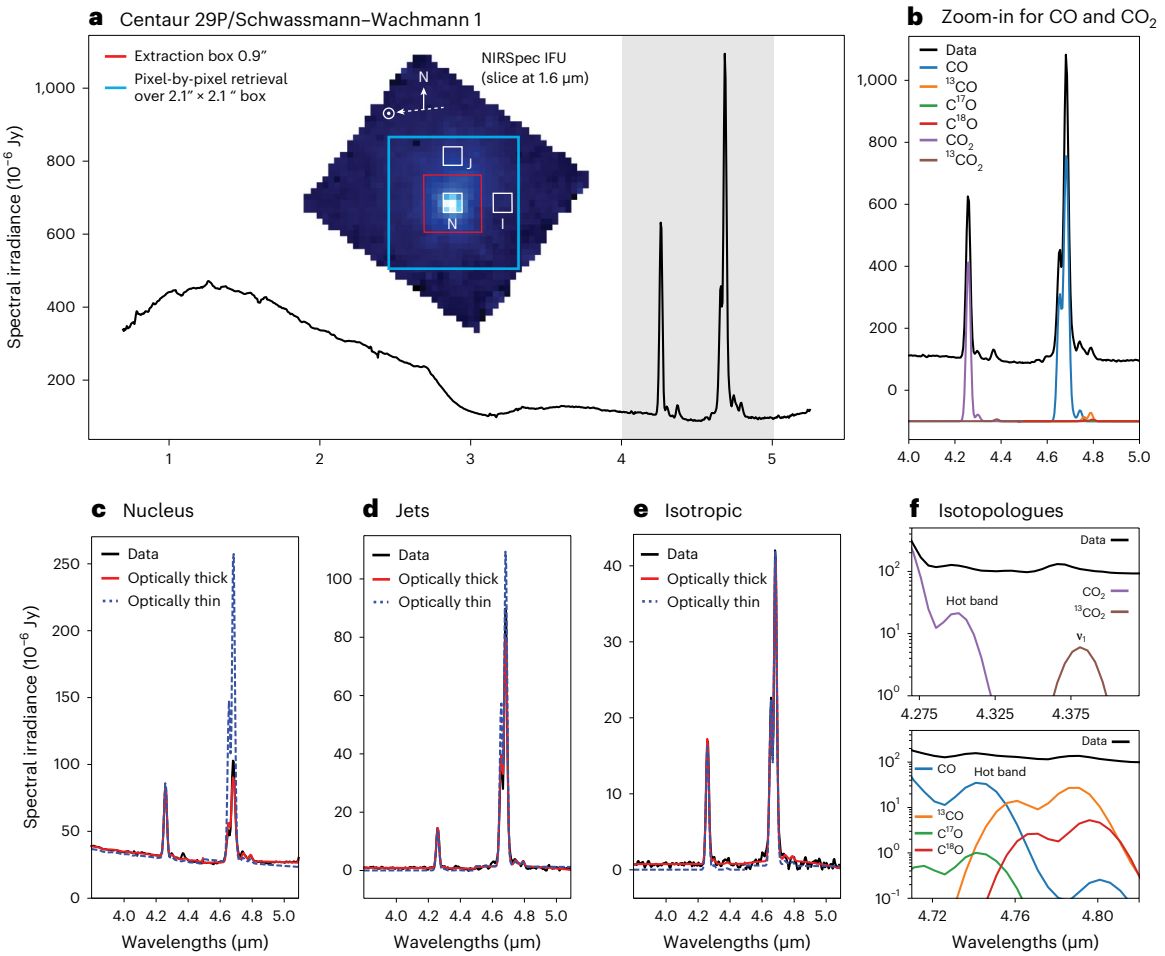

Fig. 1 | Infrared spectra of centaur 29P/Schwassmann–Wachmann 1 as measured with JWST/NIRSpec. a, Full extracted spectrum (0.6 to 5.3 μm) of centaur 29P, from a 9-spaxel-length box corresponding to 0.9″ (red box). The strong molecular emissions of CO and CO_2 and clear detections of several isotopologues of these molecules are highlighted in the grey shaded area. **b**, Zoom-in of the 4–5 μm wavelength region of the same extracted spectrum, with underlying fluorescence models for the different CO and CO_2 isotopologues as simulated with PSG[56,57]. **c**–**e**, Data extracted over a 3 × 3 spaxel region for three representative regions of the coma: the nucleus region (central white box labelled N in **a**) (**c**), the jet outgassing region (white box labelled J in **a**) (**d**) and the isotropic coma region (white box labelled I in **a**) (**e**). These data extracted from different regions of the coma show the necessity of an optically thick treatment in the fluorescence modelling. We show the best-fitting optically thick fluorescence model (red line) and the corresponding optically thin model (dashed blue line). The effects of opacity on the fluorescence emissions can be quite notable in some regions, thus requiring a specialized model as utilized here. **f**, Zoom-in of the emission features of the CO_2 (upper) and CO (lower) isotopologues with a logarithmic *y* axis to highlight the relative strength of the modelled fluorescence efficiencies. v1, vibrational emission band.

background column density for both species, which can be modelled with a common frontal jet, as previously observed for CO at millimetre wavelengths[34,35] (Fig. 2). Importantly, this modelling reconciles the 29P outgassing structure as seen observationally. Although radio measurements provide information about velocity and depth, they are less sensitive to a lateral jet in the plane of the sky (velocity nearly zero). Moreover, complementary JWST/IFU observations uniquely identify anisotropic jets projected onto the plane of sky but struggle to disentangle the isotropic outflow with a frontal jet (both mimicking a uniform column density); see 'KAMJO details' in Methods for more details.

To characterize the complex observed structure of the anisotropic outflow, we developed a three-dimensional (3D) kinematic anisotropic model of jet outgassing (KAMJO; 'KAMJO details' in Methods). Using this model, we determined that the CO frontal jet is best modelled with a half-opening angle $\delta = 45°$, azimuth $\theta = -7.9°$ and elevation $\psi = 0°$, and it is consistent with previously characterized outgassing at millimetre and submillimetre observations. The shape and orientation of the lateral CO jet is, instead, best modelled with a half-opening angle $\delta = 30°$, azimuth $\theta = -75°$ and elevation $\psi = 70°$. For the CO_2 frontal jet, we adopted the same shape and orientation as for the CO frontal jet, whereas the lateral CO_2 jets are best described with half-opening angle $\delta = 25°$, azimuth $\theta = 10°, -170°$ and elevation $\psi = -70°, 70°$. The uncertainties in the orientation and shape in the 3D KAMJO outgassing modelling are $1\sigma = \pm 5°$. For the lateral jets, we assumed that the CO north jet and CO_2 south jet point towards the observer whereas the CO_2 north jet points backwards. However, owing to mapping degeneracies, we cannot truly identify backward or forward from these observations. High-resolution kinematic information is needed for this. Independently, the different jets are clearly not overlapping spatially, which highlights the strong heterogeneous composition of the outgassing from 29P. The physical parameters ingested into KAMJO that best model the different outgassing components are reported in Table 1. The 1σ uncertainties for the production rates reported in the table are proportional to the high signal-to-noise ratio (SNR) maps derived from the spaxel-to-spaxel retrieved CO and CO_2 production rates (Supplementary Fig. 1). The map of absolute uncertainties for CO_2 ranges between SNR = 20 and 100, whereas the CO SNR map ranges between

https://doi.org/10.1038/s41550-024-02319-3

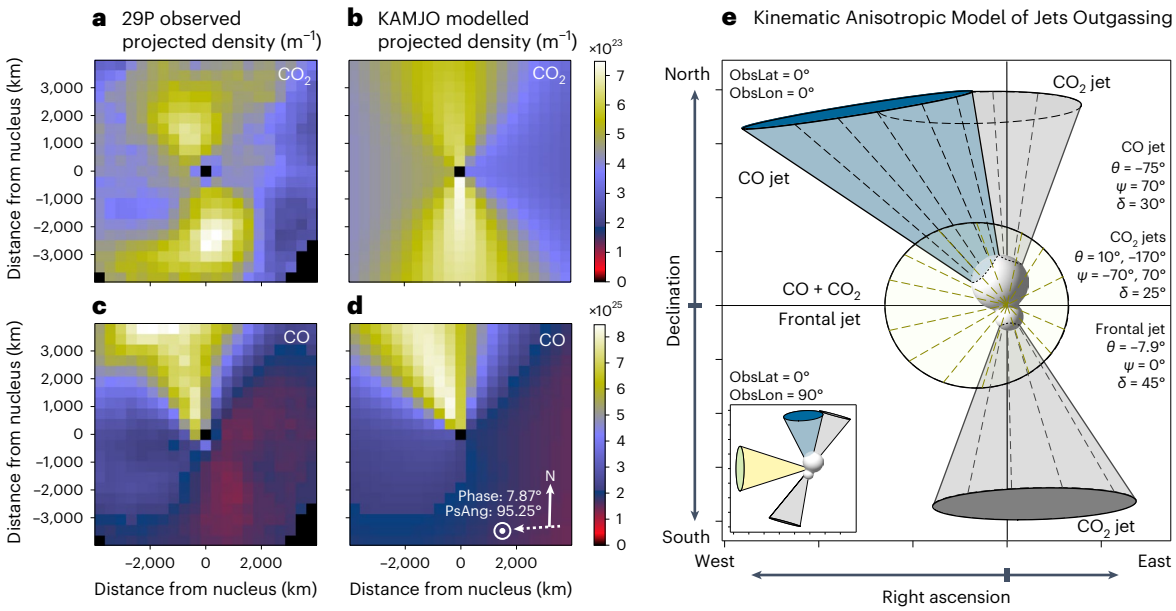

Fig. 2 | Morphologies of the CO and CO_2 outgassing jets. a,**c**, Maps of measured CO_2 (**a**) and CO (**c**) column densities (m^{-2}), divided by the inverse of the sky-plane projected distance form the nucleus $1/\rho$ (m^{-1}), as retrieved with optically thick treatment in the fluorescence modelling in PSG[56,57], in the 4–5 μm wavelength region. **b**,**d**, Maps of modelled CO_2 (**b**) and CO (**d**) column density (m^{-2}), divided by the inverse of the sky-plane projected distance from then nucleus, as the result of the 3D jet modelling (KAMJO), projected along the line of sight. **e**, Simulated view of the 3D jet modelling as seen from JWST. The strong dichotomy in the CO/CO_2 abundance ratios may be suggestive of a heterogeneous nucleus structural composition, possibly associated with a bilobed nucleus, with one lobe formed in a region where CO was more efficiently converted into CO_2 relative to the other lobe. The bilobed 3D image of the nucleus was created only for visualization purposes. ObsLat, observer latitude; ObsLon, observer longitude; PsAng, Sun's position angle; Phase, solar phase angle; θ, azimuth; ψ, elevation; δ, half-opening angle of the jet.

Table 1 | CO and CO_2 production rate (Q) and expansion velocities (v_{exp}) of the jet components, which were ingested into the 3D KAMJO model to reproduce the two-dimensional JWST anisotropic outgassing observed for 29P

	CO		CO_2		
	Frontal jet	North jet	Frontal jet	North jet	South jet
Q (s^{-1})	2.6×10^{28}	1.8×10^{28}	4.7×10^{26}	0.7×10^{26}	1.0×10^{26}
v_{exp} (ms^{-1})[a]	500	400	500	400	400

[a]Expansion velocity based on radio observations of 29P, as reported in the literature[34,35,48].

10 and 90. Owing to the uncertainties over the shape and orientation introduced in the 3D outgassing modelling, we estimated that there is about a 10% relative uncertainty (±1σ) over the production rates reported in Table 1.

Isotopic ratios

A notable aspect of the observed spectra of 29P, as shown in Fig. 1, is the clear identification of emissions for the $^{13}CO_2$, ^{13}CO, $C^{17}O$ and $C^{18}O$ isotopes across the coma. However, extracting isotopic ratios from these data is complex due to the strong opacity and the severe spectral confusion affecting these emission bands. In the inner regions of the coma, where high local densities prevail, the atmosphere starts to become optically thick, which restricts the amount of solar radiation reaching the molecules. As we are measuring the solar pumped fluorescence, this reduction in solar flux leads to a reduction of the effective fluorescence efficiencies. Correcting for this effect is not trivial, as the local opacities are proportional to the integrated column densities for each isotopologue and the individual rotational-vibrational line intensities, which vary by orders of magnitude between isotopologues and across the coma. The fluorescence models in PSG correct for the effects of opacity at the rotational-vibrational line-by-line level, yet the model utilizes an approximation to quantify and correct for the solar pump attenuation at each line[56,57]. Employing an approximation to explore minute isotopic deviations can be challenging, especially in the inner coma, where high opacities prevail. As the atmosphere becomes optically thinner away from the nucleus, these effects are largely reduced but the weaker isotopic bands become harder to properly quantify and detect.

If we assume that the isotopic ratios are common across the whole coma, then by performing multi-band multi-isotopologue retrievals across the IFU maps while specifying a specific isotopic ratio, we can explore which sets of isotopic ratios lead to a greater agreement with the data. We, therefore, performed a statistical analysis over 49 binned 3 × 3 spaxel regions and varied the isotopic ratios from a minimum of 0.1 to 10 times the telluric isotopic ratios ('Isotopic measurements' in Methods). The analysis for $^{12}C/^{13}C$ in CO_2 reveals that for 29P this ratio is consistent with telluric values within ±1σ of the distribution, as are $^{12}C/^{13}C$ and $^{16}O/^{18}O$ in CO. This analysis also showed that even though we can identify the $^{17}O/^{18}O$ signature in the observed spectra, the sensitivity is not sufficient to give a reliable quantification of that isotopic ratio. Specifically, our analysis showed that $^{12}C/^{13}C$ in CO_2 ranges between 65 and 353 (±1σ, telluric 89) and between 105 and 349 (±1σ, when weighted for SNR), $^{12}C/^{13}C$ in CO ranges between 43 and 738 (± 1σ, telluric 89) and between 42 and 720 (±1σ, when weighted for SNR), and $^{16}O/^{18}O$ in CO_2 ranges between 202 and 4,424 (±1σ, telluric 500) and between 172 and 4,393 (±1σ, when weighted for SNR). These measured ranges do not reveal a substantial divergence from telluric isotopic values.

Discussion

Of the few known active centaurs, 29P is the most active and, therefore, the most studied. It has been observed for years with multi-wavelength and multi-instrument observing campaigns[34,35,47,48,61–73], which have

monitored the dust and molecular outgassing emissions. Our knowledge of how the ices are stored in the nucleus and of the mechanisms for their release at such large heliocentric distances is, on the other hand, far from being complete.

The CO and CO_2 outgassing maps as revealed by JWST/NIRSpec show a strong dichotomy in the spatial distribution of the volatile species (Fig. 2), which raises questions about the formative origin of its nucleus. The outgassing from 29P can generally be separated into three regions of activity: (1) an insolation-driven outflow that produces the frontal jet with a production rate for $CO/CO_2 \approx 55$, (2) a northward active region with $CO/CO_2 \approx 257$ and (3) a southward active region with $CO/CO_2 \approx 0$ that is characterized by a lack of CO and a strong CO_2 jet outflow. Previous unresolved indirect photometric measurements of global comae and spectroscopic upper limits[70,74] fall within the range CO/CO_2 >15 to 90.

JWST data uniquely reveal that these active regions are dramatically different, with a CO/CO_2 ratio spanning over two orders of magnitude, yet both the north and south sides appear to have similar levels of CO_2 activity (Fig. 2). If the spatial distribution of volatile species in the coma provides direct information about how ices are stored in the nucleus[75–80], the observed heterogeneous outgassing from 29P could then be linked to the structural composition of its nucleus, which would reveal hints of its formation and evolutionary history.

One could hypothesize that these strong compositional differences are related either to dissimilar surface processing at distinct nucleus locations (evolution) or to two compositionally distinct lobes of a bilobed nucleus (formation). The former could be explained by surface erosion at distinct locations on the nucleus, which could be triggered by seasonal activity that preferentially exposes and delivers materials from the interior to the surface[81–83]. Alternatively, it could be the result of CO depletion from a polar region of a nucleus that has high obliquity[84], such that the source region is selectively exposed. The latter, instead, is strongly connected to the formation of cometary nuclei[85–89]. Bilobed structures are commonly observed in both TNO and JFC nuclei, accounting for ~70% of the objects studied[86,90,91]. This suggests that there is a general formation mechanism favouring the emergence of binarity and that the nuclei retain their bilobed shapes as they dynamically evolve into centaurs and JFCs[85,87,89]. Evolutionary processing during the centaurs' dynamical phase[86,88,92] (by, for example, collisions, outgassing, fragmentation or sublimating torques) that efficiently shapes the final nucleus of a JFC is also plausible and cannot be excluded. Thus, the heterogeneity of the volatile abundances in JFCs may be the result of such evolution. However, the drastic compositional CO/CO_2 dichotomy observed in centaur 29P suggests that here heterogeneity may also be evidence of the original formation process of its nucleus.

Taxonomical studies of CO, CO_2 and H_2O in comets has revealed contradictory results about the modelled formative region of comets[23,70,93]. Dynamically, JFCs originate predominantly from the scattered disk of the Kuiper belt, but their formative region in the early stages of Solar System formation is under discussion. JFCs are more thermally processed than LPCs, yet even though one may then presume that JFCs are depleted in hypervolatiles compared to LPCs, measurements show the abundances are not so dissimilar, with largely overlapping values[23,70] (with the caveat that CO_2 is still under-represented, although JWST is paving a new way of investigating it). This is suggestive of a common formative region for both JFCs and LPCs around the giant planets (~10 au) and over a wide range of heliocentric distances in the protoplanetary disk midplane that encompasses the H_2O, CO_2 and CO snow lines[17]. Interestingly, by comparing the CO/CO_2 volatile abundance ratios, the measurements for JFCs suggest that they perhaps formed in slightly warmer regions of the protoplanetary disk before being relocated into the hot-dynamical disk in the Kuiper belt, compared to the LPCs, which appear to have formed in colder regions[23]. For completeness, it is important to mention that for some individual comets, the CO/CO_2 ratios appear to depend on the heliocentric distance, and thus, the amount of heating a nucleus receives at the time of an observation may affect the relative production rates of these two volatiles. Thus, the measured ratio cannot be assumed to always represent nuclear ice values[70]. 29P is notable in that it maintains its heliocentric distance with a near-circular orbit so that we can eliminate the heliocentric-distance dependence as a changing parameter when modelling its nucleus for the time being (although 29P will begin moving out of its current orbit in 2038).

Water, CO and CO_2 are the most abundant volatiles in cometary ices[19,20], and $(CO + CO_2)$ is usually believed, to first approximation, to be representative of the total inorganic carbon content in cometary ices[23,93–95]. The CO/CO_2 fractional abundance shows no correlation with the total inorganic carbon content, for different dynamical families[23,70]. This indicates that if the conversion of CO into CO_2 is controlled by the fractional abundance of these two species, within the total inorganic carbon content, then comets could have formed either across the CO snow line with different gradients of CO condensation or over a wider range of heliocentric distances inside the region where amorphous ice condenses and CO is differentially trapped[94,96]. Although the latter mechanism has been less well investigated, interstellar dust-grain models show that at sufficiently high temperatures (~12 K), CO is mobile enough to reach and react with OH radicals to produce CO_2 through a high conversion efficiency chemical pathway, which allows CO_2 to dominate CO in the grain ice mantles[97,98]. At lower temperatures, instead, despite that CO_2 is still formed in significant quantities, the CO abundance usually dominates that of CO_2 (ref. 95).

The large heterogeneous CO/CO_2 abundance ratios from the active regions in 29 may then be interpreted as a dichotomy in the structural composition of its nucleus. A bilobed nucleus, with one lobe formed in a region where CO was more efficiently converted into CO_2 relative to the other lobe, is a possible interpretation.

Methods

Observations and data reduction

As part of cycle 1 programme 2416 (ref. 53), which focused on studying active centaurs (principal investigator (PI), McKay), on 20 February 2023 we used JWST/NIRSpec's IFU PRISM mode to observe centaur 29P. The object was at a heliocentric distance of 6.07 au and a distance of 5.48 au from the telescope. At the time of the observations, the solar phase angle was ~7.87° while the Sun's position angle was 95.25°.

The spectrum extracted from the NIRSpec PRISM mode gives full coverage from 0.59 to 5.29 μm, thus allowing simultaneous sampling of the three main gas species (CO, CO_2 and H_2O) and their less abundant isotopologues, with a spectral resolution of ~0.0185 μm. The NIRSpec's IFU has a FoV of 3″ × 3″, with a spatial-pixel resolution of 0.1″, which corresponded to a sky-plane projected distance of ~397.55 km at 29P. For these observations, we selected the NRSIRS^2 RAPID readout, which provides much improved noise performance and is tailored for observations of faint targets. We selected five groups per integration (with one frame per group) and six integrations per exposure. We also adopted four dither positions per integration, leading to a total of 24 integrations per exposure. The effective integration time was ~72.94 s for each dither position, and the effective exposure time of our observations was ~437.67 s.

The data analysis was performed with the Python algorithms and scripts developed by G.L.V. and S.F., which were used to analyse, calibrate and visualize JWST IFU data. These scripts are publicly available in the GitHub web page for PSG (https://github.com/nasapsg/jwst). The Python ifu.py pipeline ingests the sd3.fits files, which are one of the level-3 calibration outputs of the JWST data reduction pipeline and are freely downloadable from the Mikulski Archive for Space Telescopes at the Space Telescope Science Institute (STScI) (https://mast.stsci.edu/portal/Mashup/Clients/Mast/Portal.html). These fits

files are a 49 × 51 × 912 pixel data cube. They are wavelength calibrated in micrometres and flux calibrated in janskys. The Python ifu.py script reads the fits files for each of the four dither positions. It cleans and shifts bad pixels and combines the dithers into a single data cube. It then performs spectral extraction through aperture photometry (background subtracted) and extracts molecular column density maps of selected gas species. The column density maps were obtained over a 21 × 21 spaxel region (2.1″ × 2.1″) by adopting PSG fluorescence models and databases[56]. Maps of the spaxel-to-spaxel absolute uncertainties are reported in Supplementary Fig. 1. For each spaxel, we made an API call to the PSG server so that it performed non-resonant multi-band and multi-isotope fluorescence radiative-transfer modelling, which provided CO and CO_2 production rates and relative column densities (Supplementary Fig. 2a,d,g,j). While keeping the rotational temperature fixed at 4.5 K, we fitted a second-order polynomial function to the continuum. The isotopic abundances were also kept fixed to telluric values: $CO_2/^{13}CO_2 = 89$, $CO/^{13}CO = 89$, $CO/C^{17}O = 2{,}682$ and $CO/C^{18}O = 500$.

KAMJO details

KAMJO was developed in Python to characterize the structure of the observed CO and CO_2 jets. KAMJO can simultaneously simulate both isotropic and anisotropic outgassing for up to two jets (with the option to add more).

It runs over a four-dimensional array space. There is a 3D space of 21 × 21 × 1,200 pixels for the jet-spatial modelling component, which has a pixel spatial resolution of 0.1″ and was purposely selected to mimic the NIRSpec extracted FoV. The fourth dimension of 40 pixels is for the velocity space. It has a resolution of 50 m s^{-1}. The code ingests as input parameters the gas production rates (mol s^{-1}) for both the insolation-driven (frontal jet) and anisotropic jet components, the expansion velocities of each component in metres per second and the half-opening angle of the jets (°), which is described as an emitting cone. The 3D model is in spherical coordinates, and the direction of a jet is defined by two angles, azimuth θ (°) and elevation ψ (°), which are relative to the observer's latitude and longitude. In the 3D space, azimuth $\theta = 0°$ and elevation $\psi = 0°$ corresponds to the line of sight towards the observer. The azimuth ranges from [−180°, 180°], with negative values towards the western hemisphere and positive values towards the eastern hemisphere. The elevation ranges over [−90°, 90°], with negative values towards the south and positive values towards the north. The output of the model is the number of molecules inside each pixel (mol m^{-3}), which we projected onto the orthogonal plane of the line of sight. In this way, we recovered two-dimensional maps of the molecular column density (mol m^{-2}), which we compared with the observed data. Supplementary Fig. 2 shows the measured and modelled two-dimensional maps for CO_2 and CO column density and the residual (data-model) morphological features.

To benchmark the KAMJO model, we simulated the CO line shape as observed in the 29P average data, which was collected with the IRAM 30 m antenna from 29 December 2007 to 11 January 2011[35] when the comet was at a mean heliocentric distance Rh = 6.1 au and a mean geocentric distance $\Delta = 5.5$ au. The team used a coma model to interpret their spectra, and they identified a jet of 45° semi-aperture outgassing in the sunward direction. They extracted a jet production rate of about 2.7×10^{28} s^{-1} and an isotropic CO production rate of about 1.8×10^{28} s^{-1}. Supplementary Fig. 3 shows the 3D KAMJO simulated view of the CO jet as seen in the 29P IRAM observations, which is based on the geometry and measured production rates. There is agreement with the shape of the emission line from millimetre observations. The same figure shows the 3D simulated view of the CO and CO_2 jets and physical parameters for the JWST/NIRSpec IFU observations. We report also the simulated CO and CO_2 line profiles output by the KAMJO model for the geometry of the JWST observations.

Importantly, note that whereas the JWST data can identify anisotropic jets projected onto the plane of the sky, it is difficult to use these data to distinguish between an isotropic outflow and a broad frontal jet (azimuth <10°), since the latter would also mimic a uniform (flat) $1/\rho$ column density map. In a complementary fashion, the IRAM high-resolution data can identify frontal jets and provide information about velocity and depth, yet these data are less sensitive to a lateral jet in the plane of the sky, as its velocity is nearly zero, and any jets are diluted within the isotropic emission. The modelling results presented here reconcile the complex outgassing structure of 29P as seen by IRAM over decades of observations and by the new JWST IFU capabilities.

Finally, Supplementary Fig. 4 shows an additional output of KAMJO, namely a map of the cumulative distribution function (CDF) analysis of the modelled CO and CO_2 line profiles across the IFU. The figure shows the centre velocity v_0 (m s^{-1}), evaluated as the 50th percentile of the CDF analysis of the line profiles at each spaxel, and the full-width at half-maximum (m s^{-1}), evaluated at the 25th and 75th percentiles of the CDF analysis of the line profiles. A deviation of the centre velocity v_0 (m s^{-1}) from zero with respect to the expansion velocity is observed along the jet component. Negative values represent a delta velocity towards the observer with respect to the expansion velocity.

Isotopic measurements

Accurately quantifying isotopic ratios from these data is complex and requires a detailed study of the gas coma with specific attention to opacity and the spectral overlapping, which affect emissions in the relevant bands. Although the inner regions of the coma are dominated by higher local densities that lead to an optically thick atmosphere, the regions away from the nucleus are optically thinner but the isotopic bands become weaker and therefore harder to properly quantify and detect.

A rigorous treatment of opacity in a full non-local-thermodynamic-equilibrium fluorescence model of radiative transfer using databases containing billions of lines and a myriad of pumping and cascade processes, including non-resonance fluorescence, is extremely challenging and computationally expensive. Moreover, the local opacities are proportional to the integrated column densities for each isotopologue and the individual rotational-vibrational line intensities, which vary by orders of magnitude between isotopologues and across the coma. In PSG, an approximate approach for estimating the opacity of the pump and then correcting for it has been recently introduced, and details of the modelling can be found in the PSG handbook[57]. In summary, this approach is a first-order correction to a very complex problem and is valid only for low solar phase angles, where the integrated column density as measured by the observer also describes the column density of the incident solar flux. A core component of this approach is documenting the level of the opacity at the pump and, consequently, the transmittance at the end of column. We recognize that employing an approximation to explore minute isotopic deviations can be challenging, especially in the inner coma, where high opacities prevail.

If we assume that the isotopic ratios are common across the whole coma, then by performing multi-band multi-isotopologue retrievals across the IFU maps while specifying a specific isotopic ratio, we could then explore which sets of isotopic ratios lead to a greater agreement with the data. We, therefore, performed a statistical analysis over 49 binned 3 × 3 spaxel regions.

For each extracted spectrum, we performed retrievals by perturbing the isotopic ratios of $^{12}C/^{13}C$, $^{16}O/^{18}O$ and $^{16}O/^{17}O$ from their reference telluric values (89, 500 and 2,862, respectively) and varying them from a minimum of ×0.1 smaller up to a maximum of ×10 bigger than that value. For each iteration, we recorded the reduced χ^2 and the SNR of the retrieved multi-isotope emission. We then performed a CDF analysis over the distribution of the 49 isotopic ratios associated with the minimum of each χ^2 curve and weighted over the SNR. Supplementary Fig. 5 shows the results of this approach for the carbon isotopes in CO_2 and Supplementary Fig. 6 for the carbon and oxygen isotopes in CO.

Data availability

The data used in this analysis are publicly available from STScI's JWST archive (https://mast.stsci.edu/), cycle 1 GO, programme 2416 (ref. 53).

Code availability

The retrieval software package used in this study was PSG, which is free and available online at https://psg.gsfc.nasa.gov (refs. 56,57). The data-reduction scripts are available at https://github.com/nasapsg. Figures were made with Matplotlib v.3.2.1 (ref. 60), which is available under the Matplotlib licence at https://matplotlib.org/ (ref. 99).

References

1. Luu, J. et al. A new dynamical class of object in the outer Solar System. *Nature* **387**, 573–575 (1997).
2. Duncan, M. J. & Levison, H. F. A disk of scattered icy objects and the origin of Jupiter-family comets. *Science* **276**, 1670–1672 (1997).
3. Levison, H. F. & Duncan, M. J. From the Kuiper belt to Jupiter-family comets: the spatial distribution of ecliptic comets. *Icarus* **127**, 13–32 (1997).
4. Gladman, B., Marsden, B. G. & Vanlaerhoven, C. *Nomenclature in the Outer Solar System*. *The Solar System Beyond Neptune* (eds Barucci, M. A. et al.) 43–57 (Univ. of Arizona Press, 2008).
5. Brasser, R. & Morbidelli, A. Oort cloud and scattered disc formation during a late dynamical instability in the Solar System. *Icarus* **225**, 40–49 (2013).
6. Dones, L., Brasser, R., Kaib, N. & Rickman, H. Origin and evolution of the cometary reservoirs. *Space Sci. Rev.* **197**, 191–269 (2015).
7. Nesvorný, D. et al. Origin and evolution of short-period comets. *Astrophys. J.* **845**, 27 (2017).
8. Nesvorný, D. Dynamical evolution of the early Solar System. *Annu. Rev. Astron. Astrophys.* **56**, 137–174 (2018).
9. Volk, K. et al. OSSOS III—resonant trans-Neptunian populations: constraints from the first quarter of the outer Solar System origins survey. *Astron. J.* **152**, 23 (2016).
10. Kaib, N. A. & Sheppard, S. S. Tracking Neptune's migration history through high-perihelion resonant trans-Neptunian objects. *Astron. J.* **152**, 133 (2016).
11. Morbidelli, A. Chaotic diffusion and the origin of comets from the 2/3 resonance in the Kuiper belt. *Icarus* **127**, 1–12 (1997).
12. Tiscareno, M. S. & Malhotra, R. Chaotic diffusion of resonant Kuiper belt objects. *Astron. J.* **138**, 827 (2009).
13. Hsieh, H. H., Novaković, B., Walsh, K. J. & Schörghofer, N. Potential Themis-family asteroid contribution to the Jupiter-family comet population. *Astron. J.* **159**, 179 (2020).
14. Horner, J. & Lykawka, P. S. Planetary trojans – the main source of short period comets? *Int. J. Astrobiol.* **9**, 227–234 (2010).
15. Di Sisto, R. P., Ramos, X. S. & Gallardo, T. The dynamical evolution of escaped Jupiter trojan asteroids, link to other minor body populations. *Icarus* **319**, 828–839 (2019).
16. Sarid, G. et al. 29P/Schwassmann–Wachmann 1, a centaur in the gateway to the Jupiter-family comets. *Astrophys. J. Lett.* **883**, L25 (2019).
17. Gomes, R., Levison, H. F., Tsiganis, K. & Morbidelli, A. Origin of the cataclysmic late heavy bombardment period of the terrestrial planets. *Nature* **435**, 466–469 (2005).
18. Morbidelli, A. & Rickman, H. Comets as collisional fragments of a primordial planetesimal disk. *Astron. Astrophys.* **583**, A43 (2015).
19. Bockelée-Morvan, D. An overview of comet composition. *Proc. Int. Astron. Union* **7**, 261–274 (2011).
20. Mumma, M. J. & Charnley, S. B. The chemical composition of comets—emerging taxonomies and natal heritage. *Annu. Rev. Astron. Astrophys.* **49**, 471–524 (2011).
21. Lippi, M., Villanueva, G. L., Mumma, M. J. & Faggi, S. Investigation of the origins of comets as revealed through infrared high-resolution spectroscopy. I. Molecular abundances. *Astron. J.* **162**, 74 (2021).
22. Jewitt, D. The active centaurs. *Astron. J.* **137**, 4296 (2009).
23. A'Hearn, M. F. et al. Cometary volatiles and the origin of comets. *Astrophys. J.* **758**, 29 (2012).
24. Guilbert-Lepoutre, A., Gkotsinas, A., Raymond, S. N. & Nesvorny, D. The gateway from centaurs to Jupiter-family comets: thermal and dynamical evolution. *Astrophys. J.* **942**, 92 (2023).
25. Harrington Pinto, O. et al. First detection of CO_2 emission in a centaur: JWST NIRSpec observations of 39P/Oterma. *Planet. Sci. J.* **4**, 208 (2023).
26. Schleicher, D. G. & Farnham, T. L. In *Comets II* (eds Uwe Keller et al.) 449–469 (Univ. of Arizona, 2004).
27. Schleicher, D. G. Compositional and physical results for Rosetta's new target comet 67P/Churyumov–Gerasimenko from narrowband photometry and imaging. *Icarus* **181**, 442–457 (2006).
28. Farnham, T. L. Coma morphology of Jupiter-family comets. *Planet. Space Sci.* **57**, 1192–1217 (2009).
29. Opitom, C., Yang, B., Selman, F. & Reyes, C. First observations of an outbursting comet with the MUSE integral-field spectrograph. *Astron. Astrophys.* **628**, A128 (2019).
30. Cordiner, M. A. et al. Mapping the release of volatiles in the inner comae of comets C/2012 F6 (LEMMON) and C/2012 S1 (ISON) using the Atacama Large Millimeter/Submillimeter Array. *Astrophys. J. Lett.* **792**, L2 (2014).
31. Cordiner, M. A. et al. ALMA mapping of rapid gas and dust variations in comet C/2012 S1 (ISON): new insights into the origin of cometary HNC. *Astrophys. J.* **838**, 147 (2017).
32. Cordiner, M. A. et al. Gas sources from the coma and nucleus of comet 46P/Wirtanen observed using ALMA. *Astrophys. J.* **953**, 59 (2023).
33. Roth, N. X. et al. Rapidly varying anisotropic methanol (CH_3OH) production in the inner coma of comet 46P/Wirtanen as revealed by the ALMA Atacama Compact Array. *Planet. Sci. J.* **2**, 55 (2021).
34. Gunnarsson, M., Bockelée-Morvan, D., Biver, N., Crovisier, J. & Rickman, H. Mapping the carbon monoxide coma of comet 29P/Schwassmann-Wachmann 1. *Astron. Astrophys.* **484**, 537–546 (2008).
35. Bockelée-Morvan, D. et al. Water, hydrogen cyanide, carbon monoxide, and dust production from distant comet 29P/Schwassmann-Wachmann 1. *Astron. Astrophys.* **664**, A95 (2022).
36. A'Hearn, M. F. et al. EPOXI at comet Hartley 2. *Science* **332**, 1396 (2011).
37. Ciarniello, M. et al. The global surface composition of 67P/Churyumov-Gerasimenko nucleus by Rosetta/VIRTIS. II. Diurnal and seasonal variability. *Mon. Not. R. Astron. Soc.* **462**, S443–S458 (2016).
38. Noonan, J. W. et al. Spatial distribution of ultraviolet emission from cometary activity at 67P/Churyumov-Gerasimenko. *Astron. J.* **162**, 5 (2021).
39. Bockelée-Morvan, D. et al. Evolution of CO_2, CH_4, and OCS abundances relative to H_2O in the coma of comet 67P around perihelion from Rosetta/VIRTIS-H observations. *Mon. Not. R. Astron. Soc.* **462**, S170–S183 (2016).
40. Feaga, L. M., A'Hearn, M. F., Sunshine, J. M., Groussin, O. & Farnham, T. L. Asymmetries in the distribution of H_2O and CO_2 in the inner coma of comet 9P/Tempel 1 as observed by Deep Impact. *Icarus* **190**, 345–356 (2007).
41. Prialnik, D., Brosh, N. & Ianovici, D. Modelling the activity of 2060 Chiron. *Mon. Not. R. Astron. Soc.* **276**, 1148–1154 (1995).

42. Prialnik, D., Sarid, G., Rosenberg, E. D. & Merk, R. Thermal and chemical evolution of comet nuclei and Kuiper belt objects. *Space Sci. Rev.* **138**, 147–164 (2008).
43. Guilbert-Lepoutre, A. A thermal evolution model of centaur 10199 Chariklo. *Astron. J.* **141**, 103 (2011).
44. Guilbert-Lepoutre, A. Survival of amorphous water ice on centaurs. *Astron. J.* **144**, 97 (2012).
45. Notesco, G. & Bar-Nun, A. Enrichment of CO over N_2 by their trapping in amorphous ice and implications to comet P/Halley. *Icarus* **122**, 118–121 (1996).
46. Jenniskens, P. & Blake, D. F. Structural transitions in amorphous water ice and astrophysical implications. *Science* **265**, 753–756 (1994).
47. Paganini, L. et al. Ground-based infrared detections of CO in the centaur-comet 29P/Schwassmann-Wachmann 1 at 6.26 au from the Sun. *Astrophys. J.* **766**, 100 (2013).
48. Roth, N. X. et al. Molecular outgassing in centaur 29P/Schwassmann–Wachmann 1 during its exceptional 2021 outburst: coordinated multiwavelength observations using nFLASH at APEX and iSHELL at the NASA-IRTF. *Planet. Sci. J.* **4**, 172 (2023).
49. Romon-Martin, J., Delahodde, C., Barucci, M. A., de Bergh, C. & Peixinho, N. Photometric and spectroscopic observations of (2060) Chiron at the ESO Very Large Telescope. *Astron. Astrophys.* **400**, 369–373 (2003).
50. Bus, S. J., A'Hearn, M. F., Schleicher, D. G. & Bowell, E. Detection of CN emission from (2060) Chiron. *Science* **251**, 774–777 (1991).
51. Womack, M. & Stern, S. A. The detection of carbon monoxide gas emission in (2060) Chiron. *Sol. Syst. Res.* **33**, 187 (1999).
52. Wierzchos, K., Womack, M. & Sarid, G. Carbon monoxide in the distantly active centaur (60558) 174P/Echeclus at 6 au. *Astron. J.* **153**, 230 (2017).
53. McKay, A. et al. *Measuring Volatile Production in Active Centaurs with JWST NIRSpec*. *JWST Proposal Cycle 1* Report 2416 (NASA, 2021).
54. Jakobsen, P. et al. The Near-Infrared Spectrograph (NIRSpec) on the James Webb Space Telescope. I. Overview of the instrument and its capabilities. *Astron. Astrophys.* **661**, A80 (2022).
55. Böker, T. et al. The Near-Infrared Spectrograph (NIRSpec) on the James Webb Space Telescope. III. Integral-field spectroscopy. *Astron. Astrophys.* **661**, A82 (2022).
56. Villanueva, G. L., Smith, M. D., Protopapa, S., Faggi, S. & Mandell, A. M. Planetary Spectrum Generator: an accurate online radiative transfer suite for atmospheres, comets, small bodies and exoplanets. *J. Quant. Spectrosc. Radiat. Transf.* **217**, 86–104 (2018).
57. Villanueva, G. L. et al. *Fundamentals of the Planetary Spectrum Generator* (NASA, 2022).
58. Coplen, T. B. et al. *Compilation of Minimum and Maximum Isotope Ratios of Selected Elements in Naturally Occurring Terrestrial Materials and Reagents*. Report 01-4222 (USGS, 2001); https://pubs.usgs.gov/wri/wri014222/
59. Gordon, I. E. et al. The HITRAN2020 molecular spectroscopic database. *J. Quant. Spectrosc. Radiat. Transf.* **277**, 107949 (2022).
60. Samarasinha, N. H. & Larson, S. M. Image enhancement techniques for quantitative investigations of morphological features in cometary comae: a comparative study. *Icarus* **239**, 168–185 (2014).
61. Senay, M. C. & Jewitt, D. Coma formation driven by carbon monoxide release from comet Schwassmann–Wachmann 1. *Nature* **371**, 229–231 (1994).
62. Festou, M. C., Gunnarsson, M., Rickman, H., Winnberg, A., Tancredi, G. & Womack, M. The activity of comet 29P/Schwassmann–Wachmann 1 monitored through its CO J=2→1 radio line. *Icarus* **150**, 140–150 (2001).
63. Gunnarsson, M., Rickman, H., Festou, M. C., Winnberg, A. & Tancredi, G. An extended CO source around comet 29P/Schwassmann–Wachmann 1. *Icarus* **157**, 309–322 (2002).
64. Stansberry, J. A. et al. Spitzer observations of the dust coma and nucleus of 29P/Schwassmann-Wachmann 1. *Astrophys. J. Suppl. Ser.* **154**, 463 (2004).
65. Schambeau, C. A., Fernández, Y. R., Lisse, C. M., Samarasinha, N. & Woodney, L. M. A new analysis of Spitzer observations of comet 29P/Schwassmann–Wachmann 1. *Icarus* **260**, 60–72 (2015).
66. Ivanova, O. V., Picazzio, E., Luk'yanyk, I. V., Cavichia, O. & Andrievsky, S. M. Spectroscopic observations of the comet 29P/Schwassmann-Wachmann 1 at the SOAR telescope. *Planet. Space Sci.* **157**, 34–38 (2018).
67. Schambeau, C. A., Fernández, Y. R., Samarasinha, N. H., Woodney, L. M. & Kundu, A. Analysis of HST WFPC2 observations of centaur 29P/Schwassmann–Wachmann 1 while in outburst to place constraints on the nucleus' rotation state. *Astron. J.* **158**, 259 (2019).
68. Wierzchos, K. & Womack, M. CO gas and dust outbursts from centaur 29P/Schwassmann–Wachmann. *Astron. J.* **159**, 136 (2020).
69. Lisse, C. M. et al. 29P/Schwassmann–Wachmann 1: a Rosetta stone for amorphous water ice and CO↔CO_2 conversion in centaurs and comets? *Planet. Sci. J.* **3**, 251 (2022).
70. Harrington Pinto, O., Womack, M., Fernandez, Y. & Bauer, J. A survey of CO, CO_2, and H_2O in comets and centaurs. *Planet. Sci. J.* **3**, 247 (2022).
71. Shubina, O., Kleshchonok, V., Ivanova, O., Luk'yanyk, I. & Baransky, A. Photometry of comet 29P/Schwassmann–Wachmann 1 in 2012–2019. *Icarus* **391**, 115340 (2023).
72. Womack, M., Sarid, G. & Wierzchos, K. CO and other volatiles in distantly active comets. *Publ. Astron. Soc. Pac.* **129**, 031001 (2017).
73. Bauer, J. M. et al. The Neowise-discovered comet population and the CO+CO_2 production rates. *Astrophys. J.* **814**, 85 (2015).
74. Ootsubo, T. et al. Akari Near-Infrared Spectroscopic Survey for CO_2 In 18 comets. *Astrophys. J.* **752**, 15 (2012).
75. Villanueva, G. L. et al. The molecular composition of Comet C/2007 W1 (Boattini): evidence of a peculiar outgassing and a rich chemistry. *Icarus* **216**, 227–240 (2011).
76. Faggi, S. et al. The extraordinary passage of comet C/2020 F3 NEOWISE: evidence for heterogeneous chemical inventory in its nucleus. *Astron. J.* **162**, 178 (2021).
77. Faggi, S., Lippi, M., Mumma, M. J. & Villanueva, G. L. Strongly depleted methanol and hypervolatiles in comet C/2021 A1 (Leonard): signatures of interstellar chemistry? *Planet. Sci. J.* **4**, 8 (2023).
78. Roth, N. X. et al. The volatile composition of the inner coma of comet 46P/Wirtanen: coordinated observations using iSHELL at the NASA-IRTF and Keck/NIRSPEC-2. *Planet. Sci. J.* **2**, 54 (2021).
79. Khan, Y. et al. Comprehensive study of the chemical composition and spatial outgassing behavior of hyperactive comet 46P/Wirtanen using near-IR spectroscopy during its historic 2018 apparition. *Astron. J.* **165**, 231 (2023).
80. Dello Russo, N. et al. Post-perihelion volatile production and release from Jupiter-family comet 45P/Honda-Mrkos-Pajdušáková. *Icarus* **335**, 113411 (2020).
81. El-Maarry, M. R. et al. Surface morphology of comets and associated evolutionary processes: a review of Rosetta's observations of 67P/Churyumov–Gerasimenko. *Space Sci. Rev.* **215**, 36 (2019).
82. Cheng, A. F., Lisse, C. M. & A'Hearn, M. Surface geomorphology of Jupiter family comets: a geologic process perspective. *Icarus* **222**, 808–817 (2013).

83. Keller, H. U. et al. Insolation, erosion, and morphology of comet 67P/Churyumov-Gerasimenko. *Astron. Astrophys.* **583**, A34 (2015).
84. De Sanctis, M. C. et al. Shape and obliquity effects on the thermal evolution of the Rosetta target 67P/Churyumov-Gerasimenko cometary nucleus. *Icarus* **207**, 341–358 (2010).
85. Youdin, A. N. & Goodman, J. Streaming instabilities in protoplanetary disks. *Astrophys. J.* **620**, 459 (2005).
86. Jutzi, M. & Benz, W. Formation of bi-lobed shapes by sub-catastrophic collisions – a late origin of comet 67P's structure. *Astron. Astrophys.* **597**, A62 (2017).
87. Jutzi, M. & Asphaug, E. The shape and structure of cometary nuclei as a result of low-velocity accretion. *Science* **348**, 1355–1358 (2015).
88. Nesvorný, D. & Vokrouhlický, D. Binary survival in the outer Solar System. *Icarus* **331**, 49–61 (2019).
89. Lyra, W. & Umurhan, O. M. The initial conditions for planet formation: turbulence driven by hydrodynamical instabilities in disks around young stars. *Publ. Astron. Soc. Pac.* **131**, 072001 (2019).
90. Safrit, T. K. et al. The formation of bilobate comet shapes through sublimative torques. *Planet. Sci. J.* **2**, 14 (2021).
91. McKinnon, W. B. et al. The solar nebula origin of (486958) Arrokoth, a primordial contact binary in the Kuiper belt. *Science* **367**, eaay6620 (2020).
92. Schwartz, S. R. et al. Catastrophic disruptions as the origin of bilobate comets. *Nat. Astron.* **2**, 379–382 (2018).
93. Feldman, P. D., Festou, M. C., Tozzi, P. & Weaver, H. A. The CO_2/CO abundance ratio in 1P/Halley and several other comets observed by IUE and HST. *Astrophys. J.* **475**, 829 (1997).
94. Seligman, D. Z. et al. The volatile carbon-to-oxygen ratio as a tracer for the formation locations of interstellar comets. *Planet. Sci. J.* **3**, 150 (2022).
95. Garrod, R. T. & Pauly, T. On the formation of CO_2 and other interstellar ices. *Astrophys. J.* **735**, 15 (2011).
96. Öberg, K. I., Murray-Clay, R. & Bergin, E. A. The effects of snowlines on C/O in planetary atmospheres. *Astrophys. J.* **743**, L16 (2011).
97. Minissale, M., Congiu, E., Manicò, G., Pirronello, V. & Dulieu, F. CO_2 formation on interstellar dust grains: a detailed study of the barrier of the CO+O channel. *Astron. Astrophys.* **559**, A49 (2013).
98. Brown, M. E. & Fraser, W. C. The state of CO and CO_2 ices in the Kuiper belt as seen by JWST. *Planet. Sci. J.* **4**, 130 (2023).
99. Caswell, T. A. et al. matplotlib/matplotlib v3.1.3. *Zenodo* https://doi.org/10.5281/zenodo.3633844 (2020).

Acknowledgements

This work was supported by NASA's Goddard Astrobiology Program, Goddard's Fundamental Laboratory Research (FLaRe) and the Sellers Exoplanet Environments Collaboration. M.W. acknowledges the support received while serving at the US National Science Foundation. This work is based on observations made with the NASA/ESA/CSA JWST. The data were obtained from the Mikulski Archive for Space Telescopes at STScI, which is operated by the Association of Universities for Research in Astronomy, Inc., under NASA contract NAS 5-03127 for JWST. These observations are associated with the cycle 1 GO, programme 2416.

Author contributions

S.F. and G.L.V. analysed the data, extracted the calibrated spectra, produced the maps and performed the retrievals. A.M., PI of the observing proposal and the team, designed the observations and prepared the observational plans. D.B.-M. and N.B. assisted with the interpretation of the results by providing context related to other astronomical investigations and IRAM data. All authors contributed to the interpretation of the results and the preparation, writing and editing of the manuscript.

Competing interests

The authors declare no competing interests.

Additional information

Supplementary information The online version contains supplementary material available at https://doi.org/10.1038/s41550-024-02319-3.

Correspondence and requests for materials should be addressed to Sara Faggi.

Peer review information *Nature Astronomy* thanks Bryce Bolin and the other, anonymous, reviewer(s) for their contribution to the peer review of this work.